Offshore floating PV–DC and AC yield analysis considering wave effects

Alcañiz, A.; Monaco, N.; Isabella, O.; Ziar, H.

DOI
10.1016/j.enconman.2023.117897

Publication date
2024

Document Version
Final published version

Published in
Energy Conversion and Management

Energy Conversion and Management 300 (2024) 117897

Contents lists available at ScienceDirect

Energy Conversion and Management

journal homepage: www.elsevier.com/locate/enconman

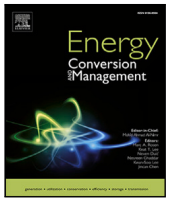

Offshore floating PV–DC and AC yield analysis considering wave effects

A. Alcañiz *, N. Monaco, O. Isabella, H. Ziar

Photovoltaic Materials and Devices Group, Delft University of Technology, Mekelweg 4 2628 CD Delft, The Netherlands

ARTICLE INFO

Keywords:
Floating photovoltaics
Offshore
Waves effect
Yield assessment
Inverter efficiency

ABSTRACT

The growing global energy demand increases the need for renewable energy sources. This increase requires land to be occupied, competing with other activities such as agriculture and residency. In such a situation, renewable energy sources expand to other environments like the ocean. However, this new scene poses some challenges, such as the effect of waves on photovoltaic (PV) performance. Consequently, this study aims to evaluate the power output of an Offshore Floating PV (OFPV) system located in the North Sea considering the effect of the waves. A 3D mechanical movement model, which has been validated with data from a real system, is developed for this purpose. A sensitivity analysis is conducted to determine how the size of fluctuations depends on the dimensions of the floater. The main outcome is that a heavy and wide floater aligned with the most common wind direction reduces angle variations. Results from DC power simulations show that sea fluctuations have a negative yet small influence on PV power production. Over the course of the year, these losses amount to just 0.1% of the annual energy yield. However, a hypothetical optimally-tilted PV system placed on water would still generate 14.6% more DC power output than the floating one. On the AC side, laboratory experiments show that these oscillations negatively affect the inverter efficiency during rough sea conditions by a decrease of over 2 percentage points compared to a still system.

1. Introduction

An expanding economy, rising population, higher need for heating and cooling, and growing urbanization are driving an increase in the world's energy demand [1]. In an effort to cover this demand sustainably, there has been unprecedented growth in renewable energy deployment, with solar energy representing around 28% of the installed renewable energy technologies globally as of 2022 [2].

These solar installations occupy a large area creating competition for land between the photovoltaic (PV) market and other essential needs such as agriculture or accommodation [3]. In this scenario, PV technology may expand to a relatively new environment: water. The application on water bodies has enormous potential [4]. If only 10% of all land-based water reservoirs were covered by PV, they would generate electricity equivalent to around 110% of all the global electricity demand [5].

Most floating PV (FPV) research and installations have focused on land-based water reservoirs [3,6]. The first commercial FPV installation was deployed in 2008 in the USA [7]. Only 5 years later, Japan installed the first MW-size FPV. However, it was not until 2019 that the first pilot FPV farm was deployed offshore [8]. This slow development is because freshwater installations cannot simply be transferred to marine areas [9].

Offshore FPV (OFPV) installations pose several benefits that make them worth exploring. During warm seasons, systems located on water display a lower operating temperature due to increased wind speed and the sea acting as a heat sink. Researchers from the Indian Institute of Technology reported that an FPV module was on average 6°C cooler than a land-based one during a reported measurement period of 17 months [10]. This resulted in an average power output 11.0% higher for the FPV module. Similar results were reported in Singapore [11]. However, the cooling effect depends on the climate and it is relatively minor in mild temperate countries like the Netherlands [12]. Other benefits of OFPV are the lack of obstacles on the sea and the low influence of the systems on the radiation balance [13]. The latter refers to the modification of the albedo by land-based solar farms, which influences the local temperature. Being ocean albedo of about 6% [14], an offshore installation does not impact it notably.

Despite the benefits, it is possible to identify several challenges that restrain the growth of FPV and OFPV in particular, such as the difficulty of maintenance, the harsh environment, the limited mechanical stability, the higher cost, and the fluctuating PV power [3,6,15,16]. Due to the need for floats, anchoring, and mooring, the cost of FPV systems can be around 4%–8% higher than that of ground-based PV [17].

An accurate yield prediction of floating PV systems is therefore needed to assess economical feasibility and investigate the technical

* Corresponding author.
E-mail address: A.AlcanizMoya@tudelft.nl (A. Alcañiz).

https://doi.org/10.1016/j.enconman.2023.117897
Received 26 April 2023; Received in revised form 2 November 2023; Accepted 15 November 2023
Available online 22 November 2023

Table 1
Previous works that estimate the yield produced by floating PV systems.

Reference	Water body	Waves model	Optoelectrical model
Goswami, 2019 [22]	Dam	None	PVSyst [23]
Suh, 2019 [24]	Dam	None	SAM [25]
Golroodbari, 2020 [26]	Sea	2D linear wave theory	Physics-based equations
Sukarso, 2020 [27]	Lake	None	SAM
Tina, 2021 [28]	Artificial basin	None	PVSyst, SAM
Ziar, 2021 [29]	Pond	None	In-house software [30]
Ghigo, 2022 [6]	Sea	WEC-Sim [31]	Fixed efficiency
Kumar, 2022 [32]	Reservoir	None	PVSyst, SAM, HelioScope [33]
Ravichandran, 2022 [34]	Sea and lake	None	HelioScope
Rahaman, 2023 [20]	Lake	None	Physics-based equations
This work	Sea	3D linear wave theory	In-house software [30]

aspects of these systems. One can find in the literature several works modelling the performance of floating systems, and more specifically focusing on thermal predictions [18–21]. However, the literature on yield modelling does not seem that extensive. Table 1 shows the most recent studies in which the yield performance of a floating system has been modelled. The approach developed in this work has also been included for comparison purposes.

One can see that most of the literature focuses on land-based water reservoirs in which the effect of waves is negligible due to their low height. Other researchers have explored the dynamic response and robustness of OFPV platforms due to wind and waves but have not studied how that movement affects the energy yield of the systems [35–38]. The only exception is the work performed by Golroodbari and van Sark [26]. They modelled the performance of a PV system on land and at sea considering the effect of sea waves, wind speed, and relative humidity. They reported an almost 13% increase in the relative annual average output DC yield of offshore systems compared to land-based ones. Although a good starting point, there are several aspects that can be put forward in their modelling approach and have been applied in this work. For instance, Golroodbari and van Sark considered only one axis of rotation for the offshore floating PV, which may underestimate the effect of wave movement. In this work, the rotation of the floating structure is modelled along two axes. Moreover, the developed mechanical model has been validated with data from a real OFPV system. These two aspects allowed the creation of guidelines for optimal floater dimensions that minimize angle fluctuations.

In Table 1, one can also observe that most of the electrical modelling has been conducted using commercial software tools. In this work, we employ a highly accurate in-house developed toolbox that has already been applied to floating systems [29]. This does not allow, as often done in the literature, to easily adapt the simple thermal models for the floating case [18]. However, the fluid dynamics-based thermal model employed in this work tends to outperform simpler thermal models [30].

Finally, it was not possible to find in literature any study regarding the losses in DC/AC conversion due to the fluctuating power produced by PV modules.

Overall, this work pursues the quantification of the power output of an offshore floating PV system considering the effect of waves on the tilt and azimuth of the modules. The wave movement will be modelled to estimate the interaction between water and the system. A mechanical model is developed and validated with real data in order to obtain the inclination of the system along the two axes. These inclinations will be input into a simulation framework to estimate the DC yield, comparing several cases. Moreover, this work aims to experimentally investigate the conversion losses due to this fluctuating DC output. Therefore, laboratory experiments will be performed to study the effect of waves on inverter efficiency. Overall the contributions of this work are as follows:

- 3D mechanical model of sea waves which results in two axes of rotation for the floating body
- Validation of the developed mechanical model using data from an OFPV system
- Development of guidelines for the optimal dimensions of a floater that decrease the angle fluctuations
- Accurate optoelectrical model using an in-house developed toolbox
- Estimation of inverter conversion losses via hardware-in-the-loop laboratory experiments

This paper is organized as follows. Section 2 explains the methodology followed through the paper. Section 3 determines the inputs chosen in this study. The results will be presented and discussed in Section 4, before concluding in Section 5.

2. Methodology

Fig. 1 provides an overview of the methodology followed in this work. The blocks have been coloured according to the subsection to which they belong. Therefore, the first two blocks correspond to the waves model (Section 2.1), orange blocks to the mechanical one (Section 2.2), the green blocks deal with the DC yield estimation (Section 2.3), and the last two blocks deal with the AC conversion (Section 2.4).

2.1. Waves model

The first step of this model consisted of deciding the type of waves to simulate. Depending on the originating mechanisms and characteristics, one can identify several wave types [39].[1] The criterion used for selection was the impact of fluctuations on the floating body. The oscillation level of a floating body is linked to the wavelength of the oscillations. Therefore, only waves with wavelengths of the same order of magnitude as the dimension of the floating body will cause a significant disturbance [40]. Amongst all options, gravity waves were selected for the modelling. Gravity waves are generated by winds that have been consistently blowing over a substantial distance [39]. They have high specific energy content [41], which facilitates wave energy modelling. Moreover, they have wavelengths between 1.5 and 900 m, which are of the same order of magnitude as the floaters in OFPV systems.

Once the type of wave is selected, its elevation and energy content need to be computed to model the interaction with the OFPV system. The interaction of sea undulations and floating bodies is highly challenging and non-linear. However, this problem can be simplified through the linear water wave theory, whose assumptions are as follows [40]:

[1] Capillary waves, infragravity waves, gravity waves, long-period waves, and tidal waves.

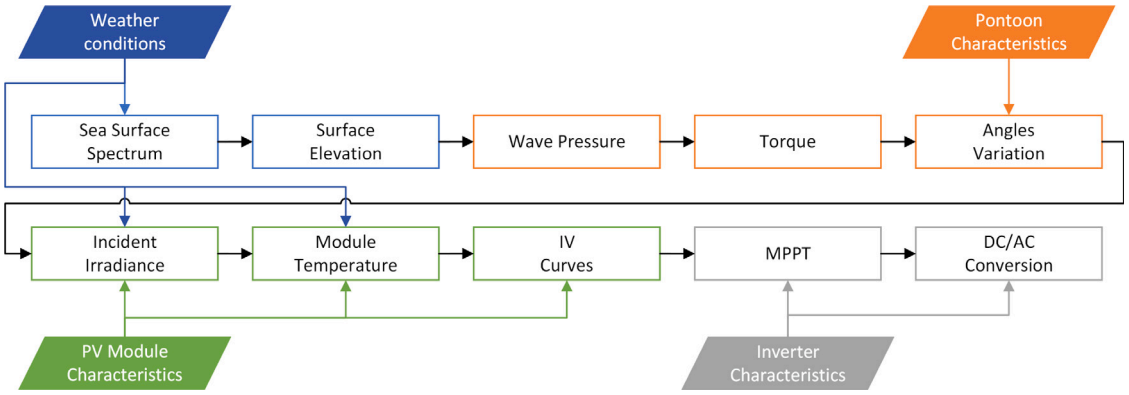

Fig. 1. Flowchart of the simulation process conducted in this work. Each colour represents a different subsection.

- The floating body is smaller than the wavelength. Large floating structures reflect and scatter waves. Nonetheless, if the wavelength is longer than the object dimensions, the wavefield is only slightly modified and wave diffraction is negligible. The object is then passively driven by the oscillations, and its presence does not notably affect the waves.
- Water is incompressible.
- Viscosity is negligible, so there is no energy loss due to water's resistance to movement.
- Coriolis force is ignored.
- The floater is at a location where deep water conditions apply.

Using the linear water wave theory, the ocean surface can be relatively simply described, by considering that the sea surface is composed of random waves of various lengths and periods. In order to factor in this randomness, a sea spectrum is employed to describe waves with different heights, durations, and shapes with limited predictability [42].

The idea of a spectrum is based on Fourier's theory that any function can be represented as the sum of an infinite series of sine and cosine functions with harmonic wave frequencies [43]. Several spectra have been suggested to represent the ocean surface, which can depend on the location. Therefore, the location of the OFPV system needs to be set. No recommended practice was found in the literature on the suitable location for an offshore floating farm. Hence, the first offshore pilot PV farm of the world was taken as a reference, which is placed on the North Sea [8]. Considering this location, the Joint North Sea Wave Observation Project (JONSWAP) spectrum was employed to model the ocean surface [44].

The system of equations explained in [45] was implemented to obtain the spectra as a function of wind speed. Fig. 2 shows the curves obtained at this step as a function of wind speed with a unique direction. The intensity of the peaks decreases with the wind speed, following a hyperbolic behaviour, typical of these spectra.

From the spectra, one can obtain the surface elevation. Recalling Fourier, the sea surface is the superposition of waves of different wavelengths and amplitudes at certain times. However, this model is developed for infinite values, which need to be discretized in order to implement it numerically. Therefore, the approach by Tucker et al. is employed, in which the amplitude components are random variables [46], as seen in Eq. (1) [47].

$$\eta(x,t) = \sum_{n=1}^{N/2} \left(a_n \cdot \cos(k_n \cdot x - \omega_n \cdot t) + b_n \cdot \sin(k_n \cdot x - \omega_n \cdot t)\right)$$
$$a_n = rn_{a_n} \cdot \sigma_S \qquad (1)$$
$$b_n = rn_{b_n} \cdot \sigma_S$$

Here, $\eta(x,t)$ is the surface elevation [m] at point x and time t, ω_n is the angular frequency [Hz] of wave n, related to the wave number

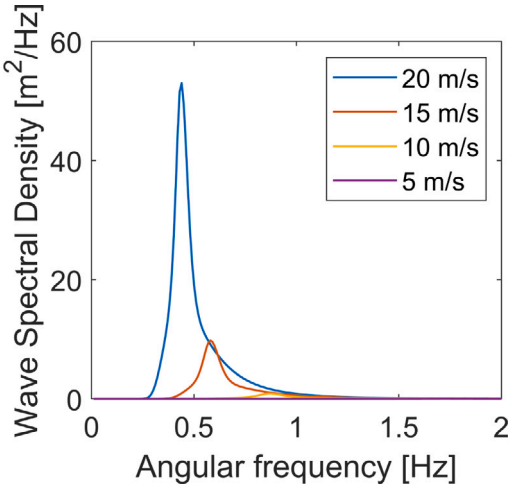

Fig. 2. JONSWAP spectra for different wind speeds.

k_n [m^{-1}] through the dispersion relation for deep water conditions, Eq. (2).

$$\omega_n^2 = g \cdot k_n \qquad (2)$$

where g is the acceleration of gravity equal to 9.81 m/s^2. a_n and b_n represent the Fourier amplitudes [m]. They are equal to the product between normally distributed random variables with zero mean rn_{a_n} and rn_{b_n}, and the standard deviation of the spectrum σ_S. N represents the discretization of the integral and is the number of angular frequencies considered, 800 in this work, from 0.01 to 8 Hz with a 0.01 Hz step.

For a more structured analysis, a sea state classification based on the surface elevation is employed. This allows to explore the effect that different sea states have on the system yield and to quantify this influence over the year. The sea will be classified based on the Douglas scale for the sea state [48]. The original scale employs 10 categories. However, this classification was too itemized for this research, so only three categories are included: calm, moderate and rough. Ranges are displayed in Table 2. The considered height is the significant wave height, an often used statistical wave measure which is the average of the highest one-third of all the waves present in an area of the sea surface [49].

2.2. Mechanical model

This subsection aims to describe the model that explains the interaction between the floating solar plant and the sea waves. For

Table 2
Sea state scale adopted in this study.

Sea State Scale	Height [m]	Description
1	0–1.25	Calm
2	1.25–2.5	Moderate
3	>2.5	Rough

this purpose, the simplified Froude–Krylov theory will be applied. The theory estimates the force that waves exert on a structure by determining pressure variations around it [50]. This approach was originally developed for submerged cylinders, but can be adapted for the case of a floating cuboid.

The application of the simplified form of this theory requires a few assumptions:

- The wave field is not affected by the floating structure.
- The floating body is considered rigid. This allows the implementation of an analytical approach, without the use of specific software packages.
- Movements on the plane parallel to the sea surface are neglected. Generally, water only moves vertically and very slightly in the direction of the wave motion [51]. It is assumed that the anchoring system reduces completely motions on the plane parallel to the sea surface as well as any rotations around the z-axis.
- The floating body is located at a height $z = 0$ with respect to the seawater level.

As previously mentioned, the Froude–Krylov approach employs the wave pressure. The pressure p [Pa] under a progressive wave can be calculated as shown in Eq. (3). In this equation, the first term refers to the dynamic pressure while the second one represents the static one.

$$p(x,z,t) = -\rho\frac{\partial\phi}{\partial t} - \rho\cdot g\cdot z \tag{3}$$

where ρ is the seawater density of 1029 kg/m^3 and ϕ is the velocity potential function [m^2/s], which is related to the surface elevation via Eq. (4).

$$\eta(x,t) = -\frac{1}{g}\frac{\partial\phi}{\partial t}\Big|_{z=0} \tag{4}$$

Knowing the surface elevation and making use of the assumption that the floating body is located at a height z = 0 m, the pressure acting on a floating body can be simplified as in Eq. (5).

$$p(x,z=0,t) = \rho\cdot g\cdot\eta \tag{5}$$

The force F [N] acting on the floater can be obtained by integrating this dynamic pressure over the area that this pressure acts on, the cuboid area (Eq. (6)). The integration range of the x-axis in the equation determines the location of the angle of rotation of the floater.

$$F = \int p\,dA = \int_{-w/2}^{w/2}\int_{0}^{l} p\,dy\,dx \tag{6}$$

where w and l are the width of the cuboid in the x- and y-axis, respectively (see Fig. 3). The upward force will be different at each location because of its dependency on the sea surface elevation. Therefore, when calculating the torque τ of this force [N m], this has to be considered as in Eq. (7).

$$\tau = F\cdot x = \int_{-w/2}^{w/2}\int_{0}^{l} p\cdot x\,dy\,dx \tag{7}$$

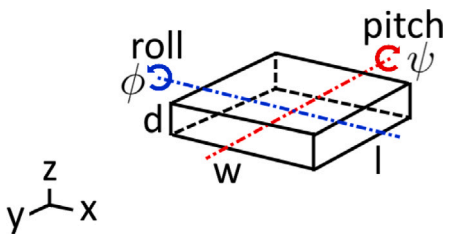

Fig. 3. Schematic of the floating body indicating the dimensions and the axes of rotation.
Source: Figure inspired by [26].

Lastly, the rotational angle of the floater θ [rad] can be obtained by using the relation between the torque, the moment of inertia [kg m^2], and the angular acceleration α [rad/s^2], written in Eq. (8).

$$\tau = I\cdot\alpha = I\cdot\frac{\partial\omega_\theta}{\partial t} = I\cdot\frac{\partial^2\theta}{\partial t^2} \tag{8}$$

When solving Eq. (8), a constant term would appear because of the indefinite integral. This term represents the value of the inclination angle at the time of the simulation. This initial inclination angle has been assumed to be 0° in the simulations since there is no information regarding its initial value. Although this can result in a slight deviation in the inclination angle, it has no statistical effect and therefore, it does not hinder the analysis.

This methodology has been developed for a single axis. However, since gravity waves follow the wind direction, which changes over time, waves hit the floater from all directions. To consider this fact, the wind is decomposed according to the North-South (NS) and East-West (EW) directions, so they are aligned with the axes of the floating body. The operations explained in the previous subsection as well as in this one are repeated for the two components so that two independent spectra are generated, from which two independent surface elevations, η_{NS} and η_{EW}, are derived and eventually two rotational angles are obtained, the roll ϕ whose rotation axis is the x-one, and the pitch ψ rotating around the y-axis. These follow common naming conventions from the literature on floating structures.

Consequently, the moments of inertia around both axes are to be calculated. The moments of inertia around the x- and y-axes passing through the centre of the cuboid shown in Fig. 3 are written in Eq. (9) [52].

$$\begin{aligned} I_x &= \frac{1}{12}m(l^2+d^2)\\ I_y &= \frac{1}{12}m(w^2+d^2)\end{aligned} \tag{9}$$

where m is the total mass [kg] and w, l, and d are the floating body dimensions [m] as illustrated in Fig. 3. In this schematic, the names of the rotational angles along each axis are also included.

The code developed thus far is included as supplementary material for those interested in modeling the mechanics of an OFPV system. The code is written in MATLAB.

2.3. Electrical model

This section models the waves' impact on the DC yield produced by an OFPV system. For this purpose, several scenarios are simulated. Apart from the OFPV oscillating scenario, two offshore systems are simulated with a fixed tilt at 0° and 34°. The former corresponds to the installation tilt of most offshore solar farms while the latter is the optimal tilt angle that maximizes the energy incident over a year at the North Sea [53]. A fourth scenario is considered inland instead of offshore with an optimal tilt as well.

The simulation framework used to reproduce the different scenarios is the PVMD Toolbox [30]. It is a physics-based simulation tool developed by the Photovoltaic Materials and Devices (PVMD) Group at Delft University of Technology. The toolbox allows users to model the performance of solar photovoltaic systems with great detail and accuracy.

Given its high accuracy, the simulation framework is computationally intensive. The computational time needed to replicate the DC output of the modules with a 1-s resolution is 4–12 h/simulated day, depending on the number of sunshine hours. One day per sea state per month is considered to reduce computational time. The performance for the overall month is obtained by multiplying the yield of each simulated day by the number of days with the same sea agitation state in that specific month.

Until now, the implemented methodology provides the roll and pitch inclination angles and assumes a constant azimuth towards the South. However, the simulation framework requires as input the tilt and azimuth at every time step. Therefore, a change of coordinates is needed to go from roll ϕ and pitch ψ to tilt α and azimuth A_M. This was done based on the generic case of panels mounted on an inclined roof [54]. The rotation that needs to be performed is expressed in Eq. (10).

$$\begin{aligned} \tan A_M &= \frac{\sin\psi}{\tan\phi} \\ \cos\alpha &= \cos\psi \cdot \cos\phi \end{aligned} \tag{10}$$

Finally, the angles were discretized to optimize the computational time by creating bins of 2° for the tilt and 5° for the azimuth.

2.4. AC conversion

This subsection explains the tests performed on a commercial string inverter connected to an in-lab-emulated OFPV system. The objective is to explore wave movement's effect on the inverter efficiency.

The input for these experiments is the current–voltage (IV) curves generated by the PVMD toolbox with a one second resolution, represented by the Maximum Power Point (MPP) coordinates P_{DC}, V_{DC} and I_{DC}. Voltage drop by cables' losses is neglected.

These curves are input to a Chroma 62100H solar array IV simulator. The device can monitor output parameters ($P_{operating}$, $V_{operating}$, and $I_{operating}$), thus allowing a dynamic study of the Maximum Power Point Tracking (MPPT) algorithm. The emulator is capable of loading up to 100 different I-V curves. Therefore, at each round of the experiment, a maximum of 100 consecutive I-V curves were fed to an inverter.

The inverter considered in this work is an SMA Inverter Sunny Boy 2.5 [55], a single-phase string inverter. Output rated power is 2.5 kVA.

A Tektronix TBS2000B Digital Oscilloscope was operated to observe and study the output signals from the inverter. Fig. 4 shows a stamp of this oscilloscope during operation. A differential and a current probe were used to monitor voltage and current, respectively. A Digilent Analog Discovery 2 data logger was used for the data extraction of P_{AC}, V_{AC} and I_{AC}. Fig. 5 shows a picture of the setup during operation.

With this setup, the inverter efficiencies can be explored. The MPPT efficiency η_{MPPT} is the ratio of the energy after the MPP tracker to the energy generated by the PV modules. The conversion efficiency η_{conv} is the ratio of the AC energy output to the DC energy input. The product of these two numbers is the inverter's total efficiency η_{tot}. Eq. (11) displays the expression for these efficiencies.

$$\begin{aligned} \eta_{mppt} &= \frac{\int_0^T P_{operating}(t)\,dt}{\int_0^T P_{DC}(t)\,dt} \\ \eta_{conv} &= \frac{\int_0^T P_{AC}(t)\,dt}{\int_0^T P_{operating}(t)\,dt} \\ \eta_{tot} = \eta_{mppt} \cdot \eta_{conv} &= \frac{\int_0^T P_{AC}(t)\,dt}{\int_0^T P_{DC}(t)\,dt} \end{aligned} \tag{11}$$

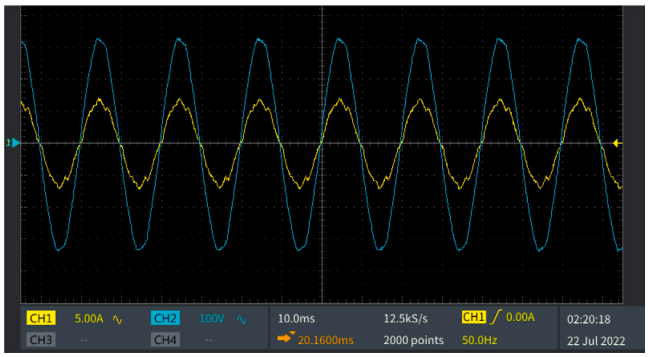

Fig. 4. Stamp of the oscilloscope during operation.

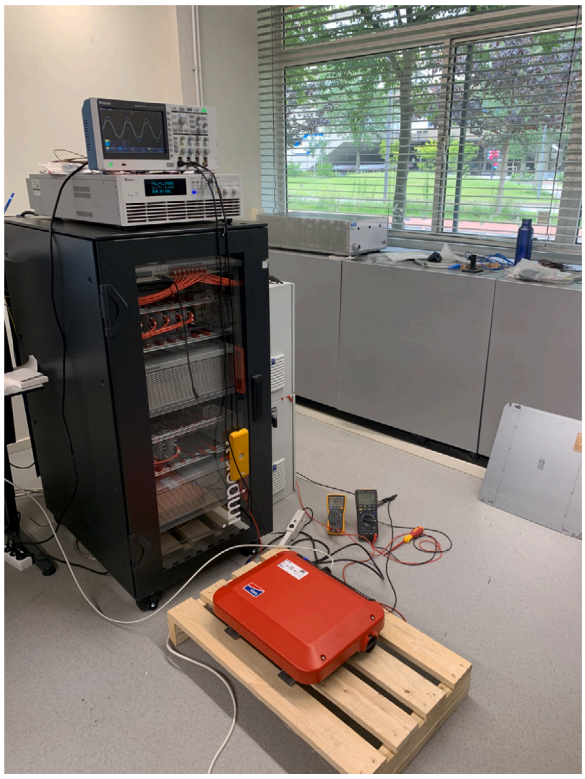

Fig. 5. Photo of the setup in operation in the laboratory.

3. Model inputs

Once the methodology is explained, this section details the inputs to the model. The first input is the location of the study. Within the North Sea, the first assumption in the waves model needs to be fulfilled: the location is at deep water conditions and subjected to high winds so that wavelengths are larger than the floating body. Moreover, the position for the development of the model is affected by the availability of data. With all these considerations, the study is located at a latitude of 53.0085° and longitude of 3.8498°, approximately 20 km from the coast (deep water condition), as shown in Fig. 6.

This research uses meteorological data from the Royal Netherlands Meteorological Institute, which is the Dutch national weather centre [57]. It provides hourly undisturbed wind and temperature data for the offshore location based on more than 40 years of collection. This research selected 2017 as a representative year after a brief exploration of the wind profiles in the latest years. The data were interpolated using the piecewise cubic method [58] to get the desired second resolution.

Fig. 6. Selected location for the OFPV system in the North Sea, and for the inland meteorological station.
Source: Image from [56].

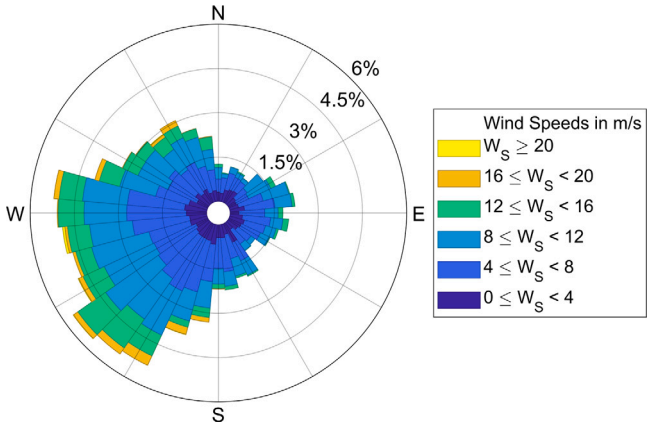

Fig. 7. Wind rose of 2017 for the location of this research, with hourly resolution.

Fig. 7 provides the wind rose of the studied year at the target offshore location. The percentages indicate how frequently that type of wind is repeated during the year, while the colours suggest wind speed levels. The wind blows mostly from the southwest, with the most frequent direction being 236°. Most of the year, the wind speed is between 5 and 10 m/s, reaching a maximum value of 23 m/s.

Unfortunately, no irradiance data were measured in the offshore meteorological station, so global horizontal irradiance was taken from an inland meteorological station located at 53.4117° 6.1992°, around 160 km from the offshore location (see Fig. 6). This data was available with a 10-min resolution, which was interpolated to get per-second data. Global irradiance was decomposed into direct and diffuse components using the BRL model [59]. These components are needed as inputs for the simulation framework. The wind speed and ambient temperature values for the inland scenario were also taken from the inland meteorological station.

An additional input to the simulation framework is the albedo. Although the state of agitation influences the sea reflection [60], the value of ocean albedo was assumed to be a constant of 0.06 [61]. In contrast, in the inland scenario, a 0.25 grassland albedo was assumed [62].

Moving on to the floating structure, there are several options available [13]. A key criterion in this research was the ease of modelling. In particular, the rigid body assumption had to be held. Therefore, a pontoon was simulated consisting of floating cubes of high-density polyethylene (HDPE). In particular, they were Sunnydock cubes manufactured by Dock Marine Europe [63]. Their dimensions are 50 cm × 50 cm × 40 cm with a weight of 6.5 kg. Each cube can withstand 87.5 kg (floatation). Although in reality these cubes allow some movement at the connection points, this is neglected in order to satisfy the rigid body assumption. As mentioned in Section 2.2, this pontoon is anchored to the sea ground and the mooring lines allow rotation of the pontoon but not displacement. A schematic of the pontoon, with the final dimensions already optimized, can be seen in Fig. 12.

Regarding the PV modules, LG400N2W-A5 monocrystalline silicon module [64] with a rated power of 400 W was selected. Considering the maximum input voltage and the rated power of the selected string inverter Sunny boy 2.5 [55], 6 modules in series can be connected per string.

4. Results

After explaining the methodology and its inputs, this section reports the results obtained at each step. The first Section 4.1 explains the outcome of the mechanical model validation using data from an OFPV system. Section 4.2 focuses on the surface elevation obtained as a result of the waves model. In Section 4.3, a sensitivity analysis on the model is performed to determine the suitable size of the system. Section 4.4 shows the interaction between the floating body and the waves through the angles' variation. Finally, results regarding the effect of waves on DC yield, module temperature, and inverter performance are explained in Sections 4.5–4.7, respectively.

4.1. Validation of the mechanical model

The applied approach, in particular up to the derivation of the rotational angles, was validated with data from an OFPV system. The sea surface elevation was also statistically validated by comparing the modelled with the measured significant wave height.

The methodology explained in Sections 2.1 and 2.2 was applied in order to emulate the OFPV system located in the North Sea. Given the stochastic nature of waves and the methodology employed, direct point-by-point comparisons of values are not reasonable. Only statistical analyses can be performed. Therefore, Fig. 8 shows two overlapped scatter plots of the modelled (in translucent red) and measured (in blue) roll and pitch for the whole measurement period. One can observe how the angles are similarly distributed in both plots. The majority of pitch and roll values are within 5° of the flat state. The distribution of modelled pitch values appears more dispersed compared to the roll due to the floater's rectangular shape. The most spread measured values could be attributed to random phenomena, not accounted for in this model, such as disturbances caused by local wind, marine life, or vessels, or to assumptions made on the dimensions and weight of the real floater.

4.2. Modelled surface elevation

This section explores the resulting waves that could have been statistically formed in 2017 with the assumed wind data and one second resolution. Fig. 9 displays examples of these results before the two axes decomposition. Sea elevation is shown for three days, one per sea state. One can observe a non-linear relation between wind speed and wave elevation: an increase in wind speed in the higher range results in a greater rise in surface elevation compared to an increase in the lower range. The lack of symmetry around 0 for the surface elevation has its origin in the random factors of Eq. (1) that can shift up and down the final summation value. Although the average monthly elevation values are relatively low (always less than 1 m), on some stormy days, the elevation exceeded 10 m.

This elevation was employed to classify the sea state into calm, moderate and rough categories for the year 2017, as explained in

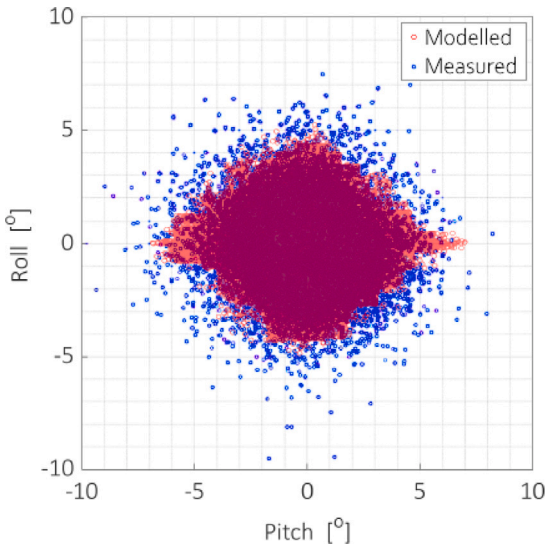

Fig. 8. Comparison between modelled and measured values of pitch and roll for an OFPV system.
Source: Figure adapted from [65].

Section 2.1. Most of the time (66%), the sea was classified as calm, while only 13% of the days were rough. Fig. 10 shows the distribution of states throughout the year, where days were classified based on daily median significant wave height and then counted for each month. The elevation is generally lower in summer and higher in winter, following the wind speed trend. No day is ranked as rough in April, May and July, while December has more rough days than calm ones.

4.3. Sensitivity analysis on sizing

As seen in Eq. (9), the inertia depends on the structure dimensions, which have a significant effect on the system dynamics. Therefore, a sensitivity analysis is performed to find the optimal size of the OFPV system. This analysis consists of exploring how sensitive the final angle variations are to the moment of inertia of the rigid floater. The objective is to map this relation in order to understand which is the optimized design for the pontoon of this offshore PV system.

Consequently, the model was run for various pontoon sizes, exploring the impact on the mean and standard deviation σ of all angles in the model. Starting with the roll and pitch, their average value was always close to 0°, hence independent of the pontoon size. Their standard deviation showed, however, more interesting trends. As observed in the top left of Fig. 11, the pitch oscillates the least when the moment of inertia of the x-axis is small, while that of the y-axis is large. That is, when the pontoon is wide but not long (the schematic of Fig. 3 is shown in Fig. 11 as well for ease of understanding). Square-shaped floaters achieve similar values although the larger and heavier the pontoon, the smaller the standard deviation. The trend of the standard deviation of the roll (top right of Fig. 11) is not so intuitive. One would have initially expected a trend similar to that of the σ pitch (smaller deviations when the pontoon is long but not wide), but that is not the case. The origin of this difference is the wind profile of the selected location. Looking at the wind rose of Fig. 7, one can see that the waves in the EW direction (y-axis of the pontoon) are larger than those in the NS one (x-axis of the pontoon). This makes the standard deviation of the roll in general higher than that of the pitch because it is affected by a combined effect of shape and mass, not only shape as happens with the pitch. The heavier the pontoon, the smaller its oscillations.

The relation of the moments of inertia with the angles is also analysed after the coordinates transformation from roll and pitch to tilt and azimuth. Few conclusions can be derived from the analysis of the azimuth since the mean is always around the South and the periodicity of the variable hinders the proper interpretation of its standard deviation. However, some information can be obtained from the mean and standard deviation of the tilt. Looking at the mean of the tilt (bottom left of Fig. 11), it is more affected by the width, although the minimum can be found for a squared and very heavy pontoon. Finally, the standard deviation of the tilt (bottom right of Fig. 11) shows a combined effect between the trends of the standard deviations of the pitch and the roll.

In summary, in this particular location, the effect of sea waves can be reduced by placing a heavy, short, and wide pontoon. This is the optimal design for two reasons. First, the heavier the floater, the smaller the fluctuations because it is harder to incline it. Second, the largest side of the pontoon is aligned with the most common wind direction. Actually, for this location, a pontoon that was aligned not with the cardinal directions but with the most common wind direction of 236° would show even lower fluctuations. This can be applied to any offshore location where the most common wind direction is known. Despite a rectangular pontoon being optimal, it was finally decided to model a squared pontoon so as to consider the intermediate scenario.

In order to determine the dimensions of this pontoon, one of the assumptions of the wave modelling needs to be considered. As stated in Section 2.1, the wavelength is assumed much longer than the dimension of the object so that the wavefield is only slightly modified by the body. But this condition is not respected for any pontoon area. Considering that 6 modules need to be connected per string, as explained in Section 3, two strings were installed per row. That is 12 modules and two string inverters for each row. Fig. 12 shows a schematic and the dimensions of the final layout. The pontoon has been added to Fig. 11 as a white diamond. Finally, floatation calculations were performed to ensure the stability of the model.

With this configuration, 3.8% of the time waves have a wavelength smaller than the width of the float. This percentage can be considered reasonable, especially considering that the elevations corresponding to such short wavelengths are minimal, and therefore have a marginal effect on the floating structure.

4.4. Inclinations due to waves

As explained in Section 2.2, the tilt and azimuth of the floating body were obtained from the sea elevation, the Froude–Krylov approach, and a coordinate transformation. The histograms in Fig. 13 show the variation in tilt probability for different wind speeds. As expected, high wind speeds increase the likelihood of significant tilting, with the tilt distributions being sharper around zero in the presence of low winds. Simulations showed that the average tilt for calm days is 0.2°, for moderate ones 1.8°, and for rough ones 4.5°. The average value over the whole year is 1.1° and the maximum simulated tilt is 52.2°.

Fig. 14 shows the connection between azimuth and wind direction. Starting with the calm sample, until around 19:00 the wind comes from the West so the pontoon oscillates between East and West without almost any disturbances. At 19:00, when the wind slowly shifts towards the North, the pontoon shows a rather irregular behaviour and does not calm until 22:00 when the pontoon oscillates between North and South. On rough days, it is harder to reach an equilibrium oscillation even when the wind is aligned with one of the axes. Higher disturbances can be observed on December 28 after 7:00 compared to the oscillations during the calm sample. This behaviour also indicates a faster change in the oscillations of the pontoon.

4.5. Waves impact on DC yield

This section focuses on the impact that waves have on the DC yield. Offshore waves influence the OFPV system yield by inclining the modules and affecting the irradiance incident on them.

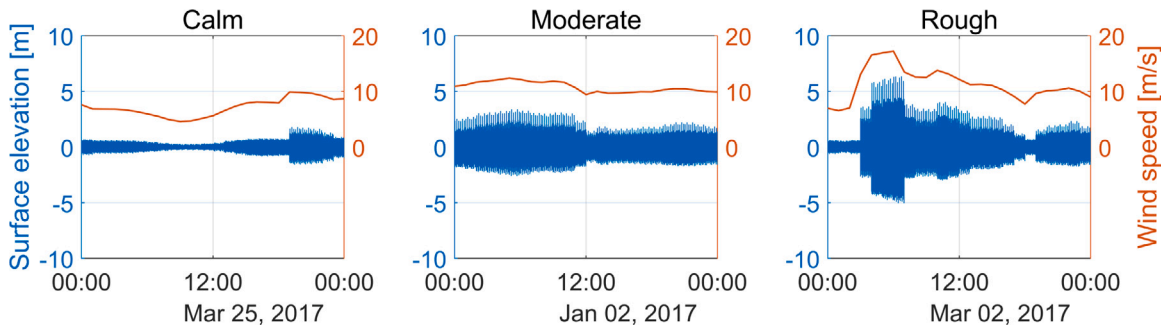

Fig. 9. Relation between surface elevation and wind speed shown for one day per sea state.

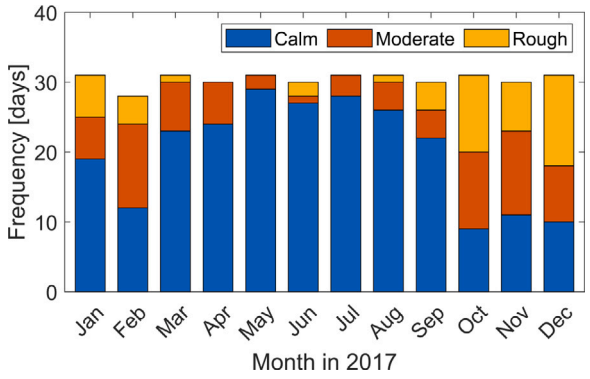

Fig. 10. Distribution of sea states over the year 2017 on daily resolution.

As a first analysis, the difference in yield is compared for three offshore scenarios: impacted by waves, fixed horizontal tilt, and fixed optimal tilt. Installing offshore solar panels with the optimal tilt is very challenging due to the mechanical stresses, so this comparison is only a theoretical analysis. Fig. 15 compares the generation of a single PV module (installed in a pontoon similar to that sketched in Fig. 12) for the three scenarios under the three sea states.

On the calm day, because of the low tilts occurring, the wave and horizontal cases follow an identical trend. As expected, the optimal tilt scenario produces more than the other scenarios. At the end of the day, the undulating scenario produces 3.62 kWh/kWp, the same as the horizontal case and 12.7% less than the optimal tilt.

On the moderate sea condition, the optimal situation also produces more. However, in some instances of time during the early morning and late afternoon, the wave case presents more significant power peaks than the optimal scenario. During these instances, the waves cause the PV panels to pose in a better orientation for that specific day and hour. Throughout the day, the fluctuations of the module with respect to the horizontal case result in an increased generation in some moments and decreased in others. Overall, the PV module with variable orientation generates 4.67 kWh/kWp, about 0.2% less than the one horizontally mounted. The module installed optimally produces +10.5% compared to the waves scenario.

Finally, a day in October is shown to investigate a rough sea. Due to the generally lower incident irradiance during rough sea conditions, the fluctuations in power generated by the case with variable orientation are of the same order of magnitude as those experienced during moderate sea conditions. On that day, the wave scenario produced 1.58 kWh/kWp, 0.4% less than the horizontal case and 42.7% less than the optimal one.

The difference in performance between the diverse sea states is investigated on all the simulated days, hence representing a whole year. The results are visible in Fig. 16. The case under the effect of the waves is always disadvantageous compared to the case with the optimal tilt, reaching an average loss of 34.1% on days with rough seas. Compared to the horizontal scenario, even in the worst-case scenario of rough sea conditions, the energy losses are impressively low, averaging just −0.4%. Considering this, the energy losses due to wave movement can be neglected in practical terms in many scenarios, as already suggested in [28].

Looking now at the yearly energy yield, the OFPV plant modelled in this study would produce 975 kWh/kWp. The fixed horizontal system would generate 976 kWh/kWp, an increase of only 0.1% compared to the fluctuating system. This value represents the overall losses due to the wave movement. As expected, the fixed optimum case is the most productive one by generating 1141 kWh/kWp, 14.6% more compared to the system affected by waves.

These trends can be graphically seen throughout the year in Fig. 17, which provides the monthly DC production. No difference can be observed between the system subjected to waves and the horizontal one, while the optimum one consistently produces more.

In summary, although the energy yield from the floating scenario is lower than that of the horizontal scenario, given the simulated conditions in this work, waves generally have a negligible impact on power production.

This study has not considered mismatch losses due to series-connected PV modules receiving different irradiance. The rigid body assumption taken in Section 2.2 subjects all PV modules to the same weather conditions. Considering however that the pontoon is composed of floating cubes, the sea agitations will most likely create movement between them leading to mismatch losses.

Using results from the literature, one can roughly estimate the mismatch losses of the system as if the PV modules in the same string received different irradiance. Kumar et al. linked the mismatch losses to the wave height based on experimental work [66]. They reported that for wave heights of 0.25, 0.5, and 1 m, the mismatch losses are around 0.1, 0.3, and 0.7%, respectively. Assuming a linear relation between these wave heights and mismatch losses, one can fit a linear interpolation between these two variables (R^2 of 95.9%) and estimate the mismatch losses for every hour using the significant wave height. Results show that the system's yearly average mismatch losses would be 1.1%, consistent with an average significant wave height of 1.5 m for the selected location. Using the results from another study obtained by Dörenkämper et al. the loss in yield due to wave-induced mismatch losses would be around 9%. The variation in mismatch losses is likely attributed to the distinct conditions simulated, including differences in floaters and locations. In both cases, the mismatch loss is higher than the loss in DC power resulting from the changing irradiance due to wave motion. These losses could be reduced during the DC to AC conversion step with a converter that employs a dynamic mismatch loss mitigation algorithm [67]. This dual input dual output converter for solar PV systems enhances power production when series-connected modules are subjected to different shading patterns, such as those created by different tilts.

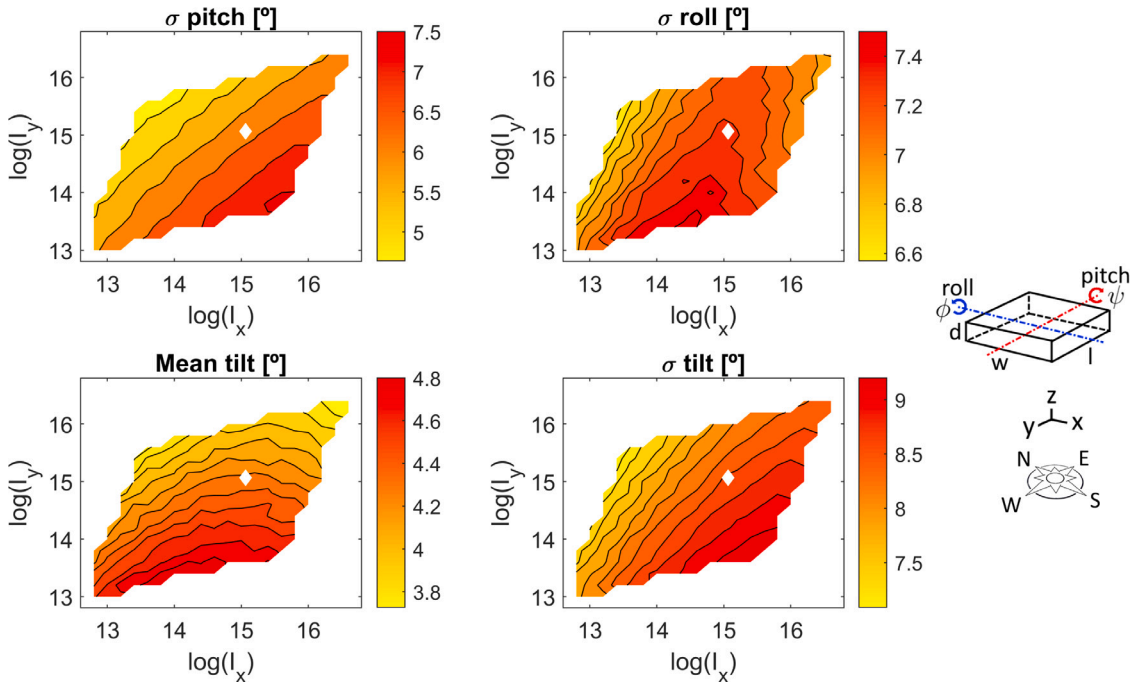

Fig. 11. Contour plots of the standard deviation of roll (top left) and of pitch (top right), mean of tilt (bottom left), and standard deviation of tilt (bottom right) as a function of the logarithm of the moment of inertia of each axis. Fig. 3 with a compass rose is shown again for ease of understanding. The pontoon modelled in this work has been represented as a white diamond in the plots.

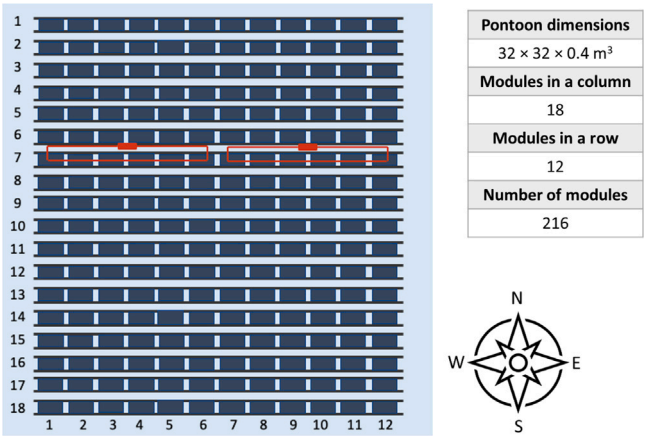

Fig. 12. Layout of the floating body facing South. The red boxes represent the two string inverters per row.

4.6. Module temperature

In order to study the difference in module temperature, a comparison is made with an inland scenario. In this subsection, three scenarios are compared: stationary optimal inland, stationary optimal offshore, and offshore subjected to waves. Ambient temperature, wind speed, and albedo differ between the inland and offshore scenarios.

Fig. 18 shows the daylight module temperature for the three investigated scenarios. Due to computational restrictions, the same approach as for the DC yield is employed: one day per month and sea state is selected as representative and it is extrapolated for each month considering the sea state distribution. The wave case shows slightly lower and less varying module temperatures than the offshore optimal one, due to the reduced irradiance incident on the PV modules. The inland system is subjected to a significantly higher temperature during the central months of the year. This difference is, in median terms, up to 5°C in some months. This trend is reversed for the coldest months of the year. This is due to water acting as a heat sink, which reduces the modules' temperature in summer but keeps them warm during winter. Additionally, the inland temperature temporal variation is more significant than the offshore one.

This difference in temperature has a significant effect on the yearly DC yield. The inland system would produce 1123 kWh/kWp, i.e. −1.7% compared to the optimal offshore application and +13.2% compared to the wave case. When contrasted with the results observed by Golroodbari and van Sark, who noted a nearly 13% increase in the DC yield for a land-based scenario compared to an offshore one [26], this study presents similar findings. This may indicate that considering two axes of rotation is not necessary in certain conditions.

Fig. 19 provides the monthly trends in 2017. From September to April, the production difference between the optimal inland and offshore scenarios is minimal. In summer, however, the advantage of installing at the sea is more evident due to the temperature effect.

Ultimately, from a technical point of view, the benefit of the offshore temperature in the ideal case leads to a gain of less than 2% in the yearly yield. Discovering if this margin can cover the higher investment cost for an offshore plant and the degradation of the components due to humidity, algae, and salt is an economic analysis that this work will not consider. However, the literature indicates that FPV can have similar or lower costs than land-based PV if there is a decrease in the cost of floaters and hybridization with hydropower [68]. The feasibility of each project will depend on the land market, installation tilt, and the drop in the price of materials for offshore installations.

4.7. Waves impact on inverter

This final section analyses the inverter results obtained in the laboratory. The objective is to quantify the inverter losses due to the fluctuating output of an OFPV system. Since the oscillations depend on the sea state condition, each condition will be studied separately and compared with a fixed horizontal OFPV system. Since the inverter

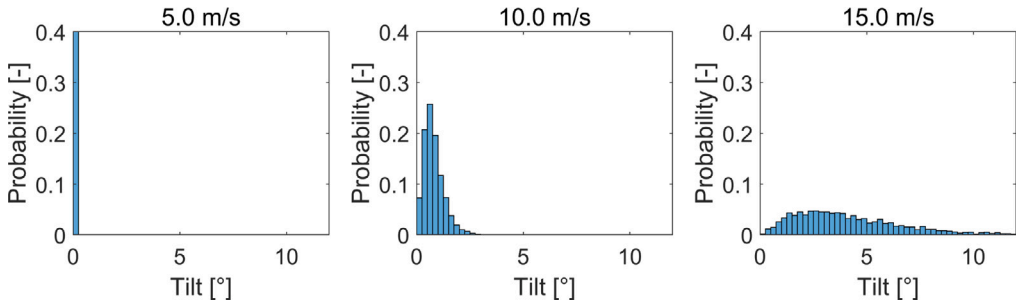

Fig. 13. Histograms of hourly tilt for different wind speeds.

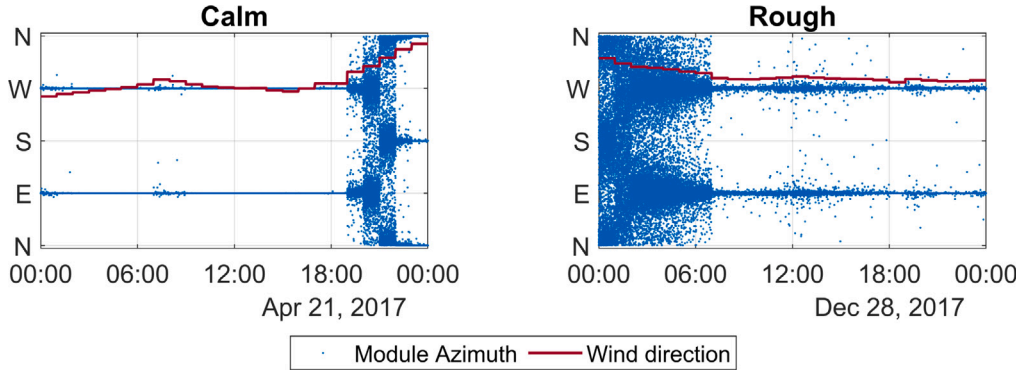

Fig. 14. Relation between wind direction and azimuth for a calm and rough day.

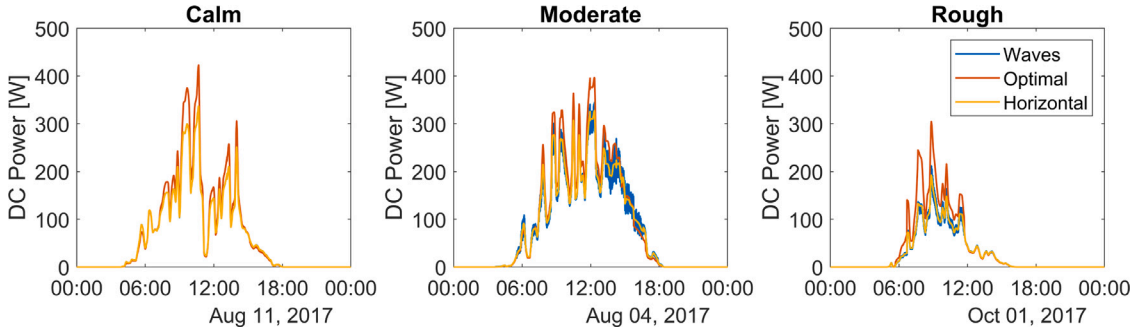

Fig. 15. DC power trend of a single PV module (rated power of 400 W) for three different sea states. Three offshore scenarios are investigated: with waves, fixed optimal, and fixed horizontal.

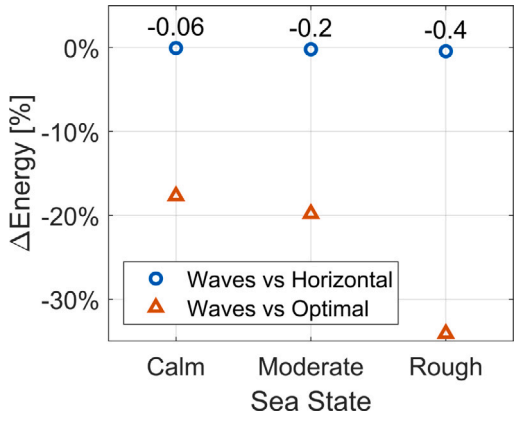

Fig. 16. Percentage difference in energy yield between the three scenarios according to the sea state.

efficiency depends on the input power produced by the modules, 9 time windows for each condition were considered in order to cover a wide range of output power values.

Fig. 20 shows one curve per condition (all with the same average power of around 1000 W) for exemplification. One can observe the undisturbed profile of DC, operating, and output power when the system is fixed or the sea is calm. The fluctuations in power are only in response to variations in irradiance. The operating and DC power curves overlap, which indicates a high MPPT efficiency. Fluctuations in power can be observed in the moderate and rough samples, with greater variability observed in the latter. These variations decrease the MPPT efficiency compared to the stationary and calm cases, although the tracker can follow quite closely the changes in DC power. The conversion efficiency does not seem much affected either by the fluctuations in power.

The average MPPT, conversion, and total efficiency have been computed for all the samples. After grouping the samples by condition, the average and standard deviation of each group have been reported in Table 3. Here, one can observe similar trends as in Fig. 20. The MPP tracker has no difficulty in finding the maximum power when there are

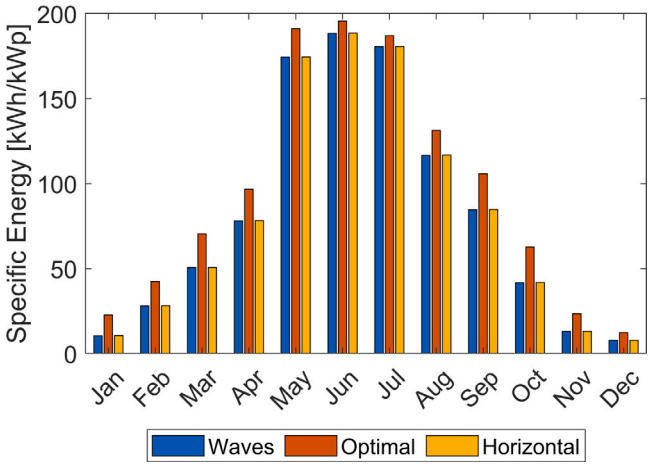

Fig. 17. Energy yield in 2017 for three offshore scenarios.

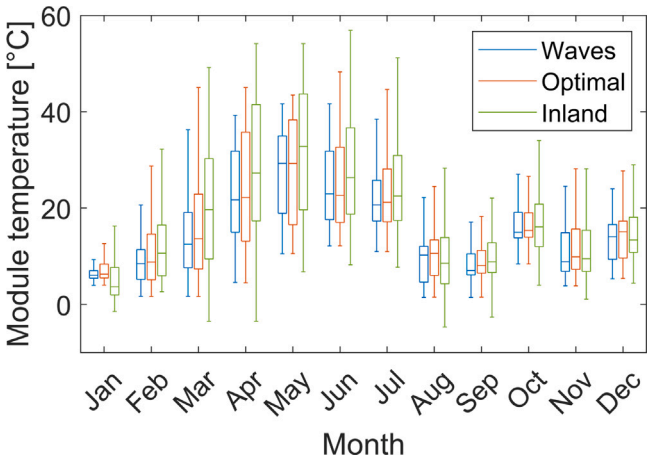

Fig. 18. Daylight module temperature in 2017 for three different scenarios: offshore considering waves, offshore steady optimal tilt, and inland steady optimal tilt.

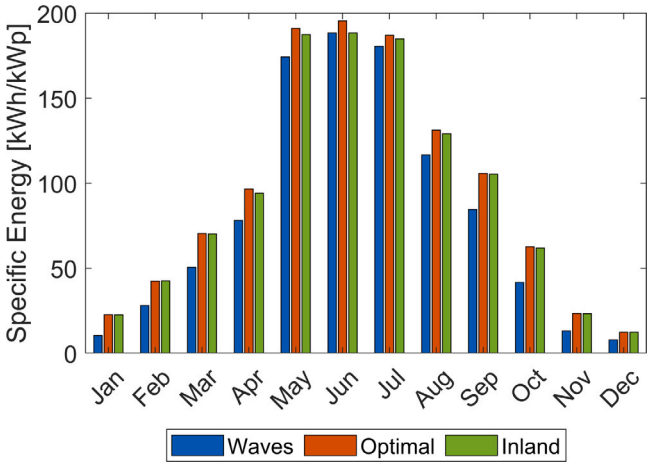

Fig. 19. Energy yield in 2017 for two offshore and one inland scenarios.

no or low fluctuations. Even when the sea state is moderate, the MPPT efficiency is barely affected. In the presence of higher fluctuations, the average MPPT efficiency drops only half a percentage point, and the standard deviation doubles. Therefore, the inverter is able to track the constantly varying maximum power point although with difficulties.

Table 3
Average values and their standard deviation for total, MPPT, and conversion efficiencies resulting from the experimental investigation.

	Total efficiency [%]	MPPT efficiency [%]	Conversion efficiency [%]
Stationary	96.0 ± 0.5	99.5 ± 0.5	96.4 ± 0.5
Calm	96.4 ± 0.3	99.3 ± 0.6	97.1 ± 0.5
Moderate	96.4 ± 0.4	99.3 ± 0.4	97.0 ± 0.2
Rough	94.1 ± 2.1	98.8 ± 1.1	95.3 ± 1.3

The conversion efficiency is affected just like the MPPT efficiency. Very similar mean and standard deviation values have been measured for the stationary, calm, and moderate samples, while the rough samples report an average conversion efficiency of about 1.5 percentage points lower and a standard deviation more than twice as large. Overall, the observed behaviour leads to an average total efficiency of 94.1% with a standard deviation of 2.1% for the rough samples. This is approximately 2 percentage points lower than the efficiency observed in the remaining cases, which have a mean efficiency ranging from 96.0% to 96.4% with a standard deviation of 0.3% to 0.5%.

In order to observe this phenomenon better, the instantaneous inverter efficiency of all the experimental data as a function of the input DC power is shown in Fig. 21. One can observe how the moderate but especially rough samples have a high variation and oscillate between high and low power values. In contrast, the stationary and calm samples are cluttered instead of dispersed. The less turbulent the sea state, the smaller this dispersion.

In summary, the inverter's total efficiency on an offshore calm or moderate day is the same as for a stationary system. An average loss of around 2 percentage points is expected during rough days compared to stationary applications. This loss is caused mostly during the DC to AC conversion process. Nevertheless, it should be noted that rough days occur especially in the winter months, with low irradiance and lower power losses compared to a clear summer day. In view of these results, one can conclude that the overall inverter losses of an oscillating system will only be slightly higher than those of a stationary one.

5. Conclusions

This work aims to simulate the performance of an offshore floating PV system. In particular, the objective was to explore the effect that the movement of waves has on the output yield and the inverter efficiency. The waves have been modelled using the JONSWAP spectrum and the interaction with the floating structure has been simulated considering two axes of rotation, an improvement in accuracy with respect to previous literature. This methodology has been validated with real data, resulting in a statistical match between modelled and measured data. A sensitivity analysis conducted on the optimal shape of the floater indicates that a heavy and rectangular floater with the widest side aligned with the most common wind direction reduces angle variations. The modelling results indicate that the waves have a negative yet negligible effect on production, leading to a decrease in the yearly energy yield of 0.1% compared to a stationary horizontal scenario. This production is however 14.6% lower than if the PV system was optimally tilted offshore. Compared to an optimally-tilted inland scenario, the decrease in production is 13.2%. This difference is due to the heat sink effect of water which can decrease the median daylight temperature by about 5 °C during the summer months. Additionally, the effect of the fluctuating PV power due to waves on the inverter efficiency has been studied for the first time in the literature, as far as the authors are aware. The experimental results show that the effect of waves on the inverter efficiency is detrimental during a rough sea, with a loss of 2 percentage points in total efficiency compared to a stationary system. Throughout the year this loss is however small considering that only 13% of the time the sea is rough.

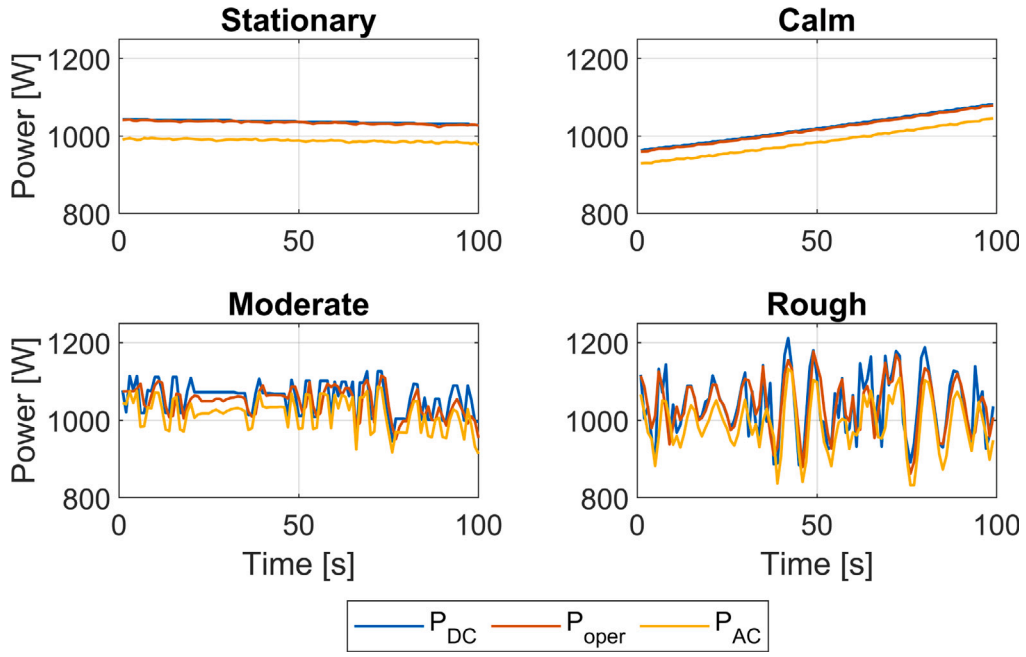

Fig. 20. P_{DC}, $P_{operating}$ and P_{AC} samples for each of the four cases analysed.

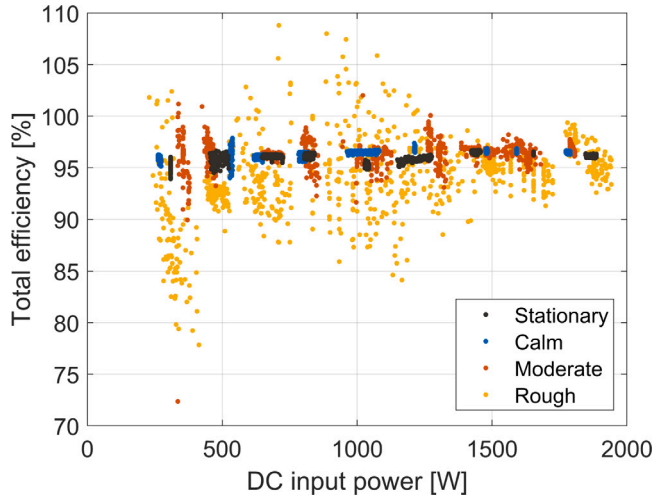

Fig. 21. Total efficiency of the inverter as a function of input DC power for all emulated samples and classified according to the four cases analysed.

CRediT authorship contribution statement

A. Alcañiz: Methodology, Software, Writing – original draft, Visualization. **N. Monaco:** Methodology, Software, Visualization. **O. Isabella:** Writing – review & editing, Supervision. **H. Ziar:** Conceptualization, Writing – review & editing, Supervision.

Declaration of competing interest

The authors declare the following financial interests/personal relationships which may be considered as potential competing interests: Alba Alcaniz reports financial support was provided by Horizon 2020.

Data availability

The authors do not have permission to share data.

Acknowledgements

The research leading to these results has received funding from the Horizon 2020 Program, under Grant Agreement 952957, Trust-PV project. Additionally, it has been developed as part of the EU-SCORES project, funded by the European Commission through the Horizon-2020 Green Deal program of CINEA. The authors are very thankful to Oceans of Energy, in particular to Dora de Jong and Álvaro de Gruijter, who were instrumental in the data collection phase, both on the selection (jointly with TU Delft) and procurement of sensors as well as the physical installation and data gathering offshore. The measured values reported in Fig. 8 of this contribution were prepared by Álvaro de Gruijter as part of his MSc thesis "Design and integration of an offshore off-grid system and an on-land system for comparison on photovoltaic performance", supervised by TU Delft.

The authors would like to thank Shagun Agarwal from the Faculty of Civil Engineering and Geosciences at TU Delft for the discussions and help provided on offshore engineering and mechanical concepts. They would also like to thank Arturo Martínez López and Stefaan Heirman for their assistance during experimental measurements.

Appendix A. Supplementary data

Supplementary material related to this article can be found online at https://doi.org/10.1016/j.enconman.2023.117897.

References

[1] IEA. Global energy review 2019. Tech. rep., Paris: IEA; 2020, URL https://www.iea.org/reports/global-energy-review-2019.
[2] IRENA G. Renewable capacity statistics 2022. International renewable energy agency; 2022.
[3] Essak L, Ghosh A. Floating photovoltaics: A review. Clean Technol 2022;4(3):752–69.
[4] Silalahi DF, Blakers A. Global atlas of marine floating solar PV potential. In: Solar, Vol. 3. MDPI; 2023, p. 416–33.
[5] Reindl T. Panel discussion in integrated PV (intro to floating PV). In: 8th world conference on photovoltaic energy conversion. 2022.
[6] Ghigo A, Faraggiana E, Sirigu M, Mattiazzo G, Bracco G. Design and analysis of a floating photovoltaic system for offshore installation: The case study of lampedusa. Energies 2022;15(23):8804.

[7] Group WB. Where Sun meets water: floating solar market report. World Bank; 2019.

[8] Oceans of Energy. A world's first: offshore floating solar farm installed at the Dutch North Sea. 2019, URL https://oceansofenergy.blue/2019/12/11/a-worlds-first-offshore-floating-solar-farm-installed-at-the-dutch-north-sea/.

[9] Hooper T, Armstrong A, Vlaswinkel B. Environmental impacts and benefits of marine floating solar. Sol Energy 2021;219:11–4. http://dx.doi.org/10.1016/j.solener.2020.10.010, URL https://www.sciencedirect.com/science/article/pii/S0038092X2031063X, Special Issue on Floating Solar: beyond the state of the art technology.

[10] Goswami A, Sadhu PK. Degradation analysis and the impacts on feasibility study of floating solar photovoltaic systems. Sustain Energy Grids Netw 2021;26:100425.

[11] Liu H, Krishna V, Lun Leung J, Reindl T, Zhao L. Field experience and performance analysis of floating PV technologies in the tropics. Prog Photovolt, Res Appl 2018;26(12):957–67.

[12] Dörenkämper M, Wahed A, Kumar A, de Jong M, Kroon J, Reindl T. The cooling effect of floating PV in two different climate zones: A comparison of field test data from the Netherlands and Singapore. Sol Energy 2021;219:15–23. http://dx.doi.org/10.1016/j.solener.2021.03.051, URL https://www.sciencedirect.com/science/article/pii/S0038092X21002395, Special Issue on Floating Solar: beyond the state of the art technology.

[13] Ziar H. Floating solar stations. In: 10 breakthrough ideas in energy for the next 10 years. 2021, p. 30–43.

[14] Baradei SE, Sadeq MA. Effect of solar canals on evaporation, water quality, and power production: An optimization study. Water 2020;12(8):2103.

[15] Makhija AS, Bohra S. Performance and degradation analysis for different solar photovoltaic technologies under hot and humid environment: A review. Prog Energy 2023.

[16] Zhao S, Low YM, Rodríguez-Gallegos CD, Reindl T. Potential root causes for failures in floating PV systems. In: ASME 2023 42nd international conference on ocean, offshore and arctic engineering. American Society of Mechanical Engineers Digital Collection; 2023, p. 11.

[17] Almeida RM, Schmitt R, Grodsky SM, Flecker AS, Gomes CP, Zhao L, Liu H, Barros N, Kelman R, McIntyre PB. Floating solar power could help fight climate change—let's get it right. Nature 2022;606(7913):246–9.

[18] Micheli L. The temperature of floating photovoltaics: Case studies, models and recent findings. Sol Energy 2022;242:234–45. http://dx.doi.org/10.1016/j.solener.2022.06.039, URL https://www.sciencedirect.com/science/article/pii/S0038092X22004650.

[19] Kjeldstad T, Lindholm D, Marstein E, Selj J. Cooling of floating photovoltaics and the importance of water temperature. Sol Energy 2021;218:544–51.

[20] Rahaman MA, Chambers TL, Fekih A, Wiecheteck G, Carranza G, Possetti GRC. Floating photovoltaic module temperature estimation: Modeling and comparison. Renew Energy 2023;208:162–80.

[21] Lindholm D, Selj J, Kjeldstad T, Fjær H, Nysted V. CFD modelling to derive U-values for floating PV technologies with large water footprint. Sol Energy 2022;238:238–47.

[22] Goswami A, Sadhu P, Goswami U, Sadhu PK. Floating solar power plant for sustainable development: A techno-economic analysis. Environ Prog Sustain Energy 2019;38(6):e13268.

[23] PVsyst SA. 2023, https://www.pvsyst.com/, Accessed: 2023-06-15.

[24] Suh J, Jang Y, Choi Y. Comparison of electric power output observed and estimated from floating photovoltaic systems: A case study on the hapcheon dam, Korea. Sustainability 2019;12(1):276.

[25] NREL. System advisor model. 2023, https://sam.nrel.gov/, Accessed: 2023-06-15.

[26] Golroodbari SZ, van Sark W. Simulation of performance differences between offshore and land-based photovoltaic systems. Prog Photovolt, Res Appl 2020;28(9):873–86.

[27] Sukarso AP, Kim KN. Cooling effect on the floating solar PV: Performance and economic analysis on the case of west Java province in Indonesia. Energies 2020;13(9):2126.

[28] Tina GM, Scavo FB, Merlo L, Bizzarri F. Comparative analysis of monofacial and bifacial photovoltaic modules for floating power plants. Appl Energy 2021;281:116084.

[29] Ziar H, Prudon B, Lin F-Y, Roeffen B, Heijkoop D, Stark T, Teurlincx S, de Senerpont Domis L, Goma EG, Extebarria JG, et al. Innovative floating bifacial photovoltaic solutions for inland water areas. Prog Photovolt: Res Appl 2021;29(7):725–43.

[30] Vogt MR, Tobon CR, Alcañiz A, Procel P, Blom Y, Din ANE, Stark T, Wang Z, Goma EG, Etxebarria JG, Ziar H, Zeman M, Santbergen R, Isabella O.

[31] Ruehl K, Ogden D, Yu Y-H, Keester A, Tom N, Forbush D, Leon J, Grasberger J, Husain S. WEC-Sim v5.0.1. 2022, http://dx.doi.org/10.5281/zenodo.7121186, URL https://zenodo.org/badge/latestdoi/20451353.

[32] Kumar NM, Chakraborty S, Yadav SK, Singh J, Chopra SS. Advancing simulation tools specific to floating solar photovoltaic systems–Comparative analysis of field-measured and simulated energy performance. Sustain Energy Technol Assess 2022;52:102168.

[33] Solar A. Helioscope. 2023, https://helioscope.aurorasolar.com/, Accessed: 2023-06-15.

[34] Ravichandran N, Ravichandran N, Panneerselvam B. Comparative assessment of offshore floating photovoltaic systems using thin film modules for Maldives islands. Sustain Energy Technol Assess 2022;53:102490.

[35] Trapani K, Millar D. Hydrodynamic overview of flexible floating thin film PV arrays. In: Proceedings of the 3rd Offshore Energy and Storage Symposium, Valletta, Malta. 2016, p. 13–5.

[36] Al-Yacouby A, Halim ERBA, Liew M. Hydrodynamic analysis of floating offshore solar farms subjected to regular waves. In: Advances in manufacturing engineering: selected articles from ICMMPE 2019. Springer; 2020, p. 375–90.

[37] Lee G-H, Choi J-W, Seo J-H, Ha H. Comparative study of effect of wind and wave load on floating PV: Computational simulation and design method. J Korean Soc Precis Eng 2019;18(11):9–17.

[38] Diendorfer C, Haider M, Lauermann M. Performance analysis of offshore solar power plants. Energy Procedia 2014;49:2462–71.

[39] Toffoli A, Bitner-Gregersen EM. Types of ocean surface waves, wave classification. Encyclopedia Marit Offshore Eng 2017;1–8.

[40] Grotmaack R. Small rigid floating bodies under the influence of water waves. Res Lett Inf Math Sci 2003;5:143–57.

[41] Holthuijsen L. Waves in coastal and oceanic waters. New York, NY: Cambridge University Press; 2007.

[42] Dawson TH. Offshore structural engineering. Prentice-Hall; 1983.

[43] Pecher A, Kofoed JP. Handbook of ocean wave energy. Springer Nature; 2017.

[44] Hasselmann K, Barnett TP, Bouws E, Carlson H, Cartwright DE, Enke K, Ewing J, Gienapp A, Hasselmann D, Kruseman P, et al. Measurements of wind-wave growth and swell decay during the Joint North Sea Wave Project (JONSWAP). Ergaenzungsheft Dtsch Hydrogr Z Reihe A 1973.

[45] Yu Y, Pei H, Xu C. Parameter identification of JONSWAP spectrum acquired by airborne LIDAR. J Ocean Univ China 2017;16(6):998–1002.

[46] Tucker M, Challenor PG, Carter D. Numerical simulation of a random sea: a common error and its effect upon wave group statistics. Appl Ocean Res 1984;6(2):118–22.

[47] Vazirizade SM. An intelligent integrated method for reliability estimation of offshore structures wave loading applied in time domain (Ph.D. thesis), University of Arizona; 2019, Available at https://repository.arizona.edu/bitstream/handle/10150/636592/azu_etd_17617_sip1_m.pdf?sequence=1.

[48] Owens EH. Sea conditions. In: Beaches and coastal geology. Encyclopedia of earth sciences series, Boston: Springer US; 1982, p. 722–804.

[49] Collins III CO. Typhoon generated surface gravity waves measured by NOMAD-type buoys. University of Miami; 2014.

[50] Mani J. Coastal hydrodynamics. PHI Learning Pvt. Ltd.; 2012.

[51] Pinet PR. Essential invitation to oceanography. Jones & Bartlett Publishers; 2014.

[52] Spiegel MR. Manual de fórmulas y tablas matemáticas. U.S.A.: McGraw-Hill Book Co; 1986.

[53] Jacobson MZ, Jadhav V. World estimates of PV optimal tilt angles and ratios of sunlight incident upon tilted and tracked PV panels relative to horizontal panels. Sol Energy 2018;169:55–66.

[54] Smets AH, Jäger K, Isabella O, Swaaij RA, Zeman M. Solar energy: The physics and engineering of photovoltaic conversion, technologies and systems. UIT Cambridge; 2015.

[55] SMA. Sunny boy 1.5/2/2.5 - datasheet. 2021, URL https://files.sma.de/downloads/SBxx-1VL-40-DS-en-51.pdf.

[56] Google Maps. N53.00848 E3.84971. 2022, URL https://www.google.nl/maps/place/53%C2%B000'30.5%22N+3%C2%B050'59.0%22E/@52.9956374,2.5582527,368001m/data=!3m1!1e3!4m5!3m4!1s0x0:0x92158b03b3ef01b5!8m2!3d53.00848!4d3.84971 (accessed 15/06/2022).

[57] KNMI. KNW Atlas, URL https://www.knmi.nl/research/observations-data-technology/projects/knw-atlas.

[58] Fritsch FN, Carlson RE. Monotone piecewise cubic interpolation. SIAM J Numer Anal 1980;17(2):238–46. http://dx.doi.org/10.1137/0717021.

[59] Boland J, Huang J, Ridley B. Decomposing global solar radiation into its direct and diffuse components. Renew Sustain Energy Rev 2013;28:749–56.

[60] Golroodbari S, van Sark W. On the effect of dynamic albedo on performance modelling of offshore floating photovoltaic systems. Sol Energy Adv 2022;2:100016.

[61] Sinnett G, Feddersen F. Observations and parameterizations of surfzone albedo. Methods Oceanogr 2016;17:319–34.

[62] Liu H, Tu G, Dong W. Three-year changes of surface albedo of degraded grassland and cropland surfaces in a semiarid area. Chin Sci Bull 2008;53(8):1246–54.

[63] Marine D. [Link]. 2020, URL https://uploads-ssl.webflow.com/5e2394bfb966d96dd886cadf/5e2cd9f18c2b174d9dbee2ae_Sunnydock.pdf.

[64] LG. LG400N2W-A5 datasheet. 2017, URL https://www.lg.com/us/business/download/resources/BT00002151/LG400N2W-A5.pdf.

[65] de Gruijter Á. Design and integration of an offshore off-grid system and an on-land system for comparison on photovoltaic performance. 2023.

[66] Kumar M, Nysted VS, Otnes G, Kjeldstad T, Roosloot N, Selj JH. Impact of water waves on the output power of floating PV systems on water bodies. In: 8th world conference on photovoltaic energy conversion. 2022.

[67] Thanikanti SB, B PK, S D, Aljafari B, Colak I. A dynamic mismatch loss mitigation algorithm with dual input dual output converter for solar PV systems. Sol Energy Mater Sol Cells 2023;251:112163. http://dx.doi.org/10.1016/j.solmat.2022.112163, URL https://www.sciencedirect.com/science/article/pii/S0927024822005803.

[68] Micheli L, Talavera DL, Marco Tina G, Almonacid F, Fernández EF. Techno-economic potential and perspectives of floating photovoltaics in Europe. Sol Energy 2022;243:203–14. http://dx.doi.org/10.1016/j.solener.2022.07.042, URL https://www.sciencedirect.com/science/article/pii/S0038092X22005217.